

Supplementary Information

Codesign of an Integrated Metal-Insulator-Semiconductor Photocathode for Photoelectrochemical Reduction of CO₂ to Ethylene

Chanyeon Kim^{1,2,3,6}, Alex J. King^{1,2,3}, Shaul Aloni^{2,4}, Francesca M. Toma^{2,3}, Adam Z. Weber^{2,5}, and
Alexis T. Bell^{1,2,3*}

¹Department of Chemical and Biomolecular Engineering, University of California, Berkeley,
California 94720.

²Liquid Sunlight Alliance, Lawrence Berkeley National Laboratory, Berkeley, California 94720.

³Chemical Sciences Division, Lawrence Berkeley National Laboratory, Berkeley, California 94720.

⁴The Molecular Foundry, Lawrence Berkeley National Laboratory, Berkeley, California 94720.

⁵Energy Technologies Area, Lawrence Berkeley National Laboratory, Berkeley, California 94720.

⁶Department of Energy Science & Engineering, Daegu Gyeongbuk Institute of Science and
Technology, Daegu 42988, Republic of Korea

*Correspondence to: alexbell@berkeley.edu (A.T. Bell)

Supplementary Figures

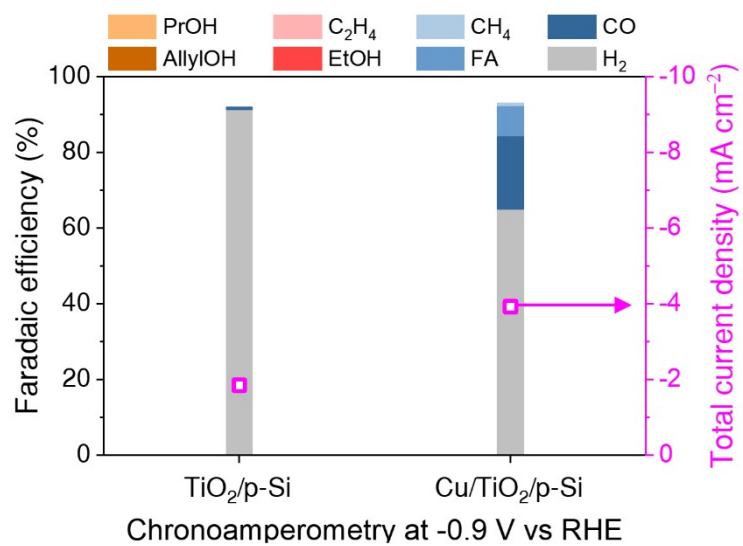


Figure S1. PEC CO₂R performance of TiO₂/p-Si and Cu/TiO₂/p-Si

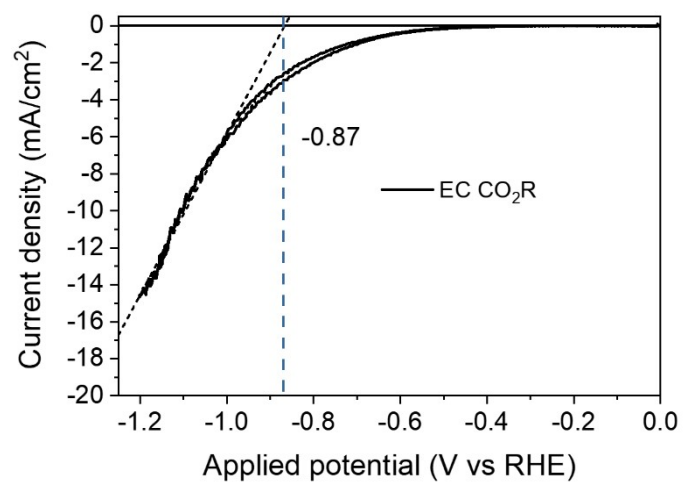


Figure S2. Estimation of onset potential of EC CO₂R on Cu layer.

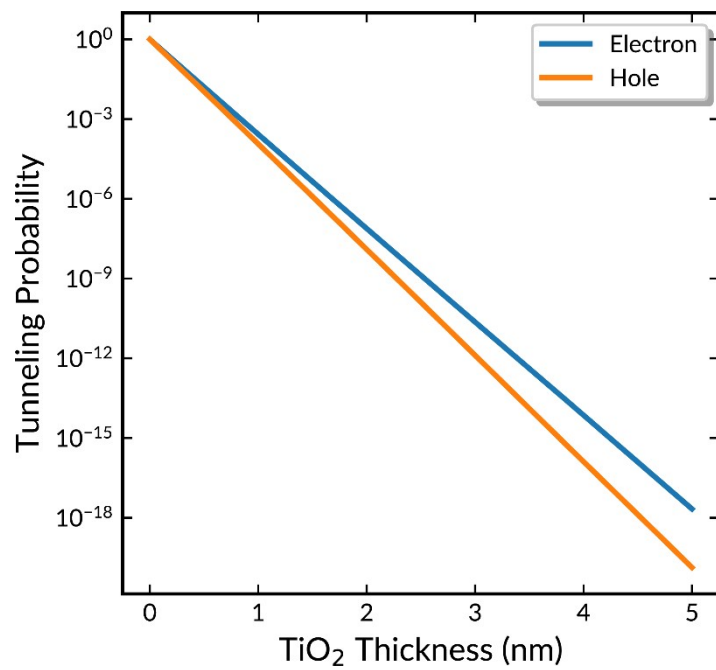


Figure S3. Modeled tunneling probability for electrons (blue) and holes (orange) against TiO₂ thickness.

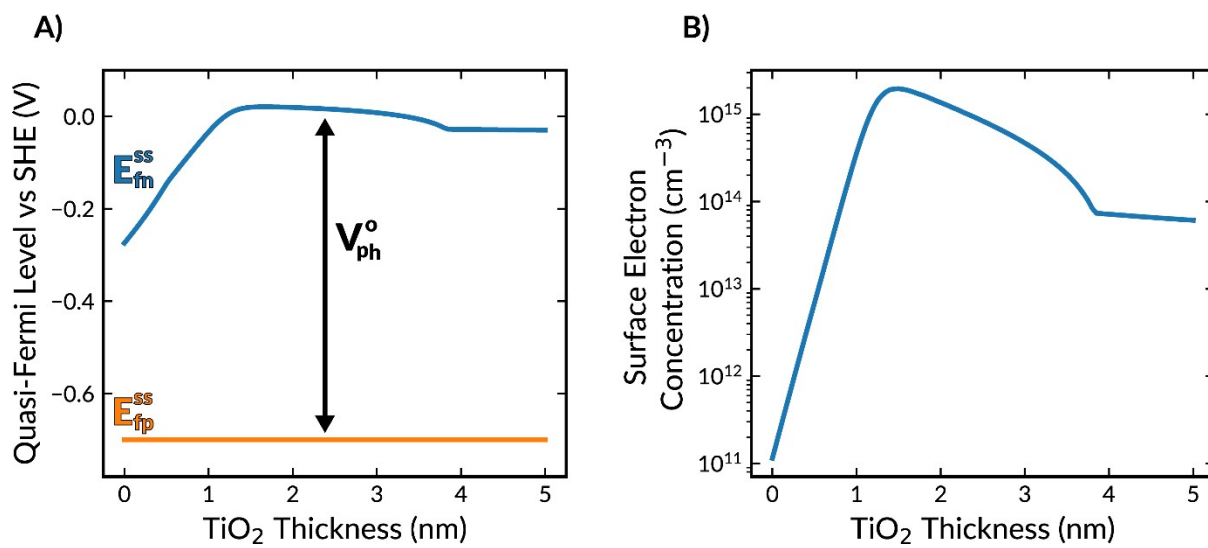


Figure S4. Modeled ideal photovoltage (V_{ph}^o), quasi-Fermi levels, and electron concentration. (A) quasi-Fermi level at the semiconductor surface for electrons (blue) and holes (orange) and (B) surface electron concentration as a function of insulator thickness.

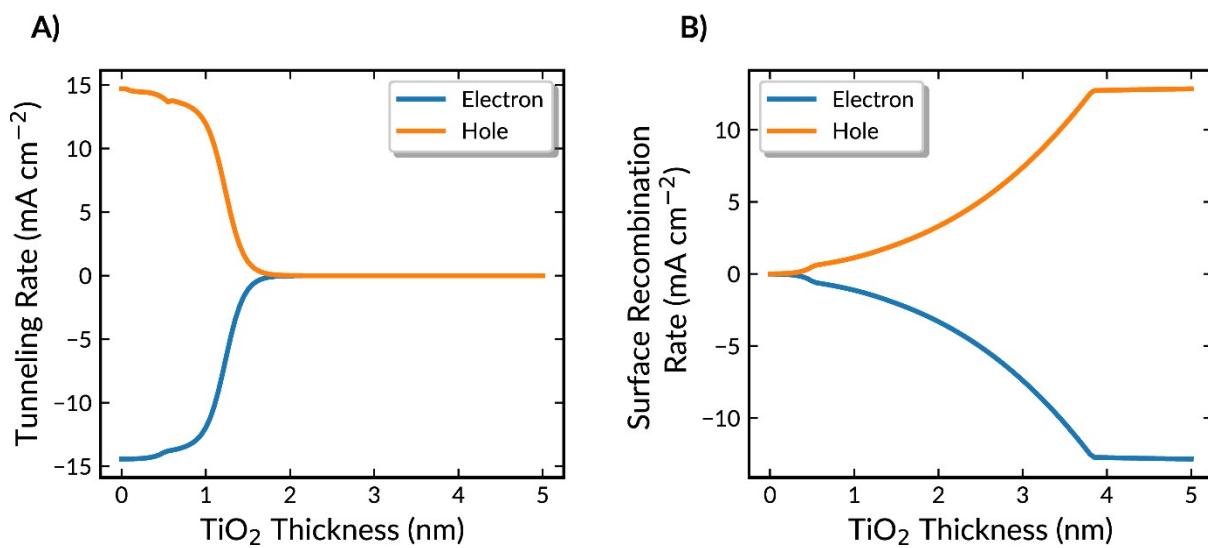


Figure S5. Modeled tunneling and surface recombination rate. Electron (blue) and hole (orange) (A) tunneling rate and (B) surface recombination rate as a function of insulator thickness.

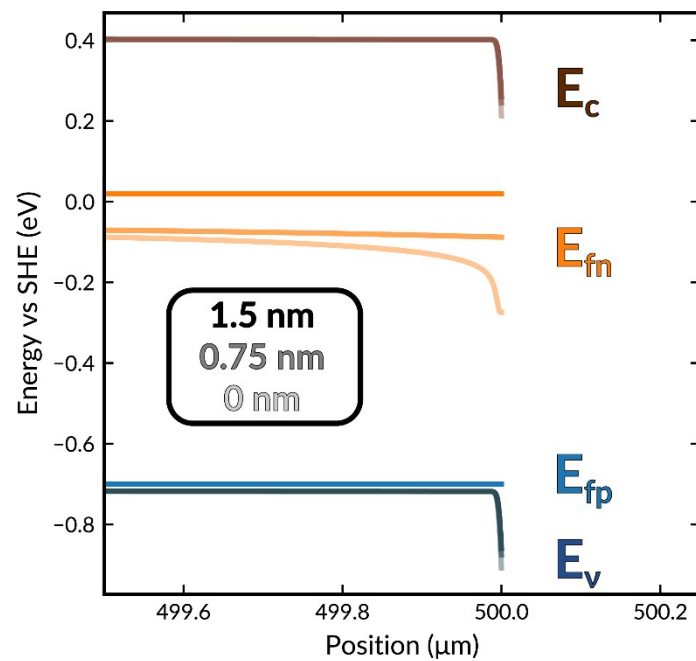


Figure S6. Band Bending Near Si Surface at Various TiO₂ Thicknesses. Band energy diagram for Cu/TiO₂/p-Si photoelectrode at varying insulator thicknesses at 0 mA cm⁻². E_c , E_{fn} , E_{fp} , and E_v are the semiconductor conduction band, quasi-Fermi level of electrons, quasi-Fermi level of holes, and the semiconductor valence band, respectively.

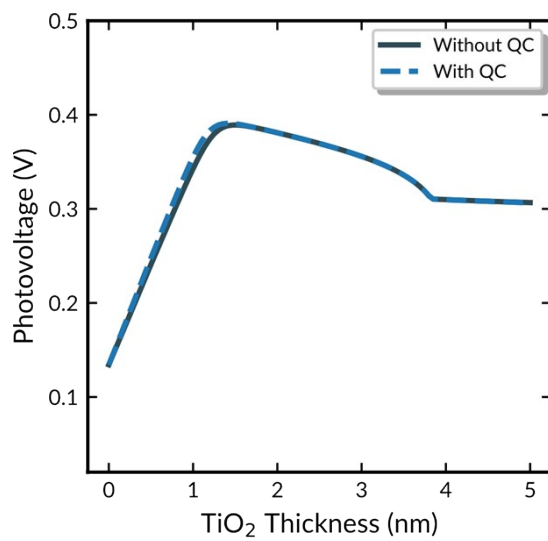


Figure S7. Impact of Quantum Confinement on Simulation Results is Negligible. Photovoltage as a function of insulator thicknesses at 0 mA cm^{-2} with and without the effects of quantum confinement on the bandgap of TiO₂ (3.5 eV and 3.8 eV without and with quantum confinement (QC), respectively)¹.

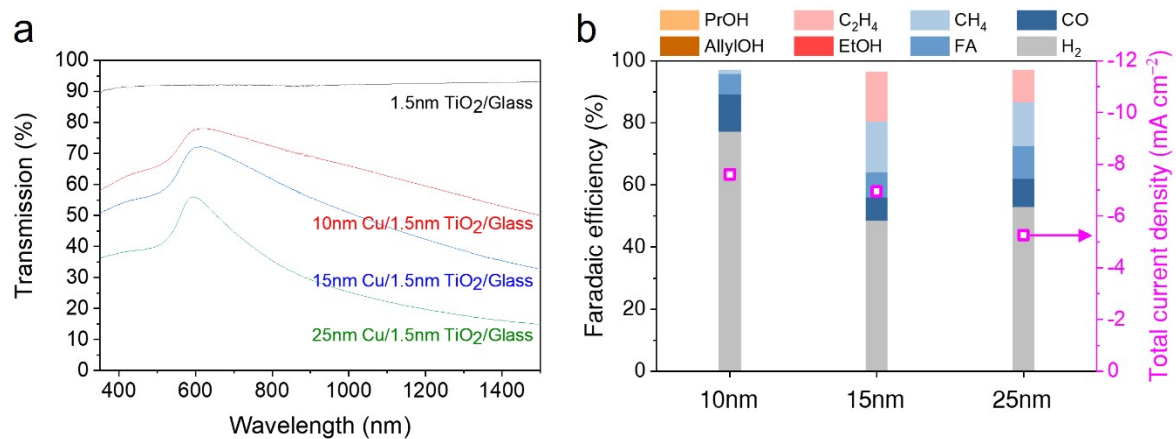


Figure S8. Optimal thickness of Cu layer for PEC CO₂R under wet-side illumination. Effect of Cu thickness on **a** light transmission and **b** PEC CO₂R performance under wet-side illumination. PEC CO₂R performance was evaluated using 0.1M CsHCO₃ electrolyte at -0.9 V vs RHE.

We deposited a thin layer of ionomer on the Cu catalyst of the MIS structure with the aim of determining the optimal loading of both Sustainion and Nafion for ethylene production (see Figure S7). As the loading of Sustainion on the MIS (S/MIS) increased up to $1.8 \mu\text{g}/\text{cm}^2$, the photocurrent increased but the ethylene selectivity remained nearly identical to that obtained in the absence of the ionomer layer, indicating an increased rate of ethylene production. However, when the loading amount was greater than $4.5 \mu\text{g}/\text{cm}^2$, HER dominated, likely due to limited mass transport of CO_2 through the thick ionomer layer. Thus, the optimal loading of Sustainion was $1.8 \mu\text{g}/\text{cm}^2$. Similarly, for a Nafion loading greater than $1.8 \mu\text{g}/\text{cm}^2$ on the MIS (N/MIS) HER dominated once again probably due to the limited CO_2 mass transport.

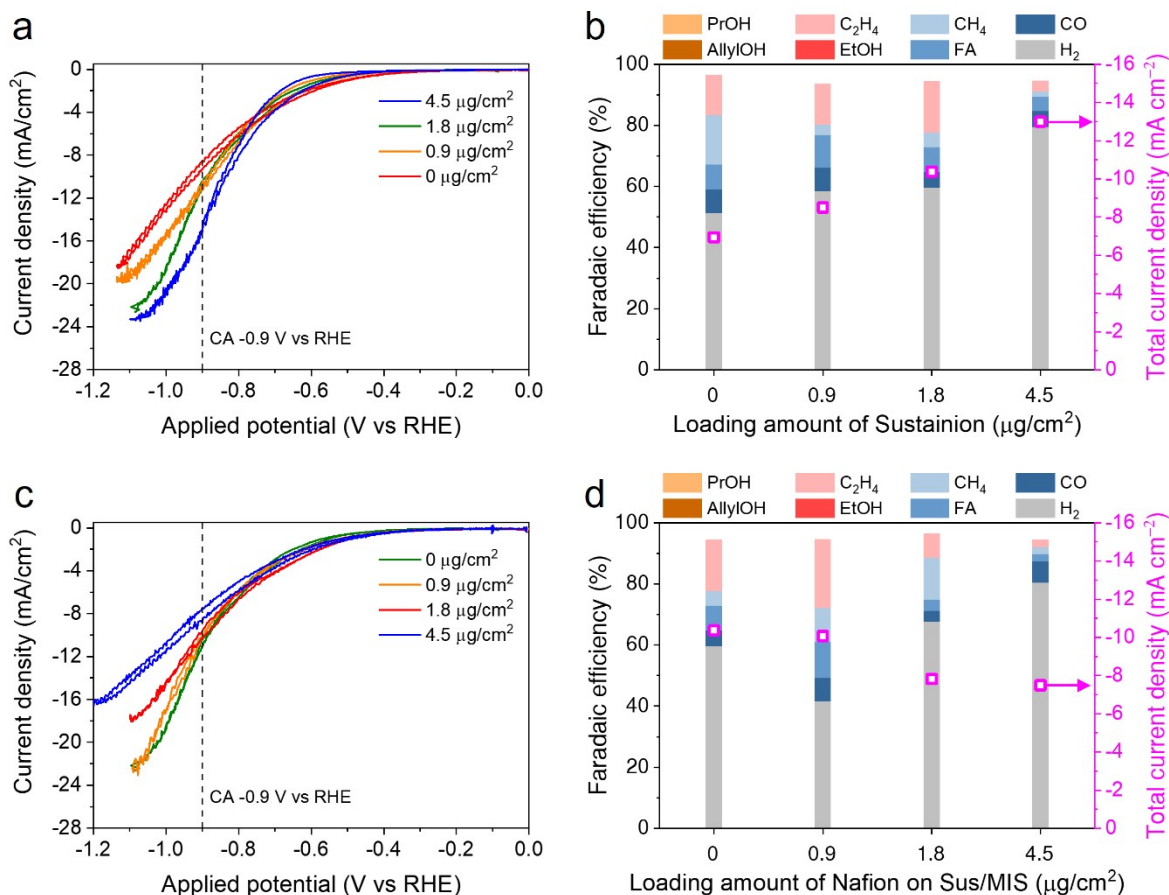


Figure S9. Optimal loading amount of ionomer for PEC CO_2R using MIS photocathode under wet-side illumination. Effect of Sustainion loading on PEC CO_2R using Sustainion coated MIS during **a** CV and **b** CA at -0.9 V vs RHE in the presence of 0.1 M CsHCO_3 electrolyte. Effect of Nafion loading on PEC CO_2R performance using Nafion/Sustainion/MIS during **c** CV and **d** CA at -0.9 V vs RHE in the presence of 0.1 M CsHCO_3 electrolyte.

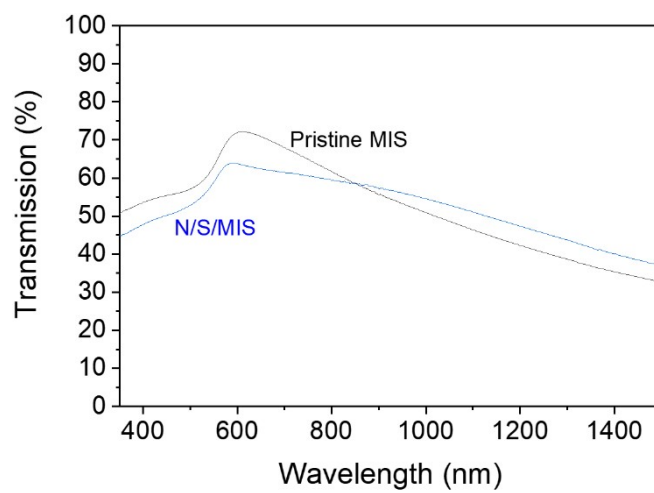


Figure S10. Light absorption by ionomer bilayer.

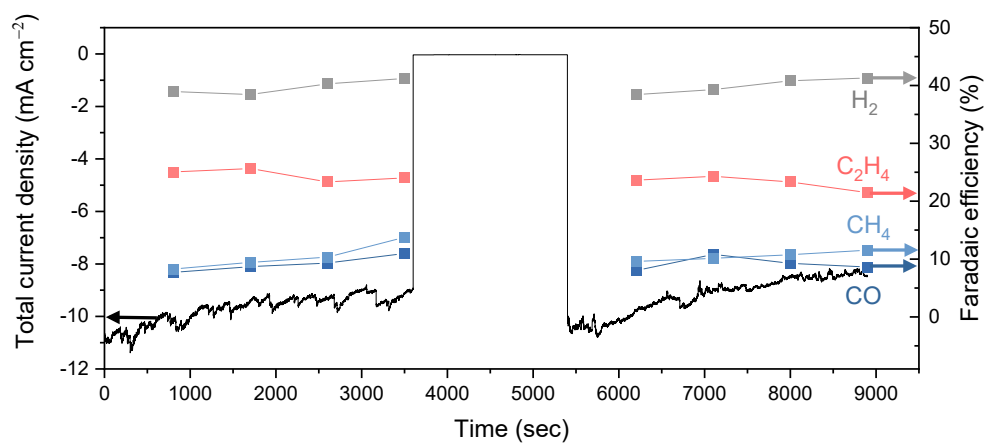


Figure S11. Stability of Product Selectivity. Sequential PEC CO₂R with or without light irradiation using Naf/Sus/MIS photocathode.

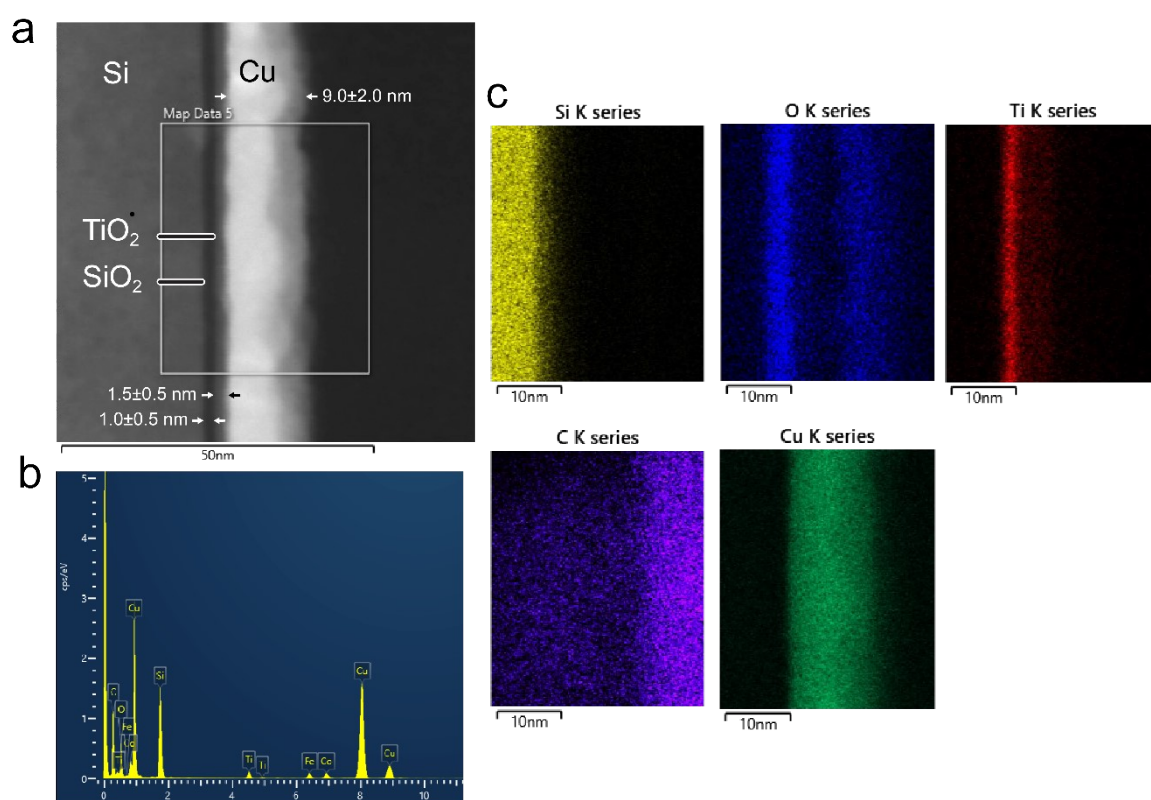
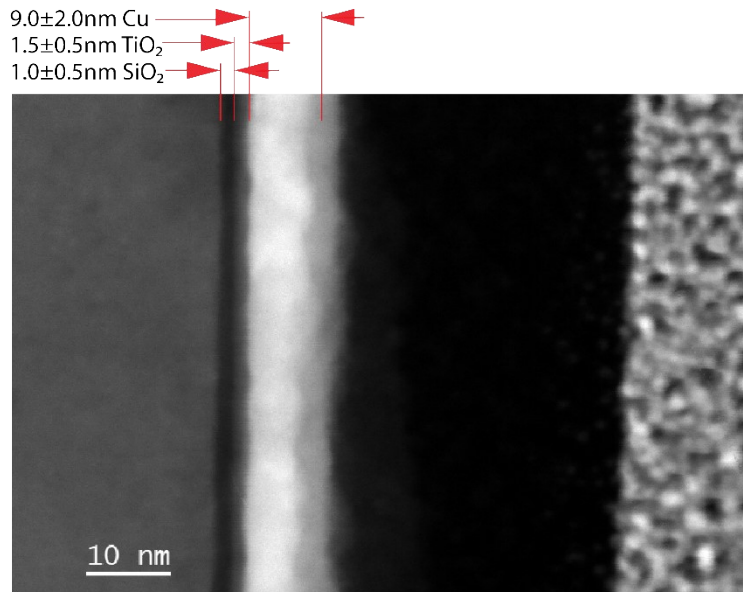


Figure S12. Characterization of MIS sample. (a) Scanning transmission electron microscopy (STEM) image of fresh Cu/TiO₂/p-Si sample. **(b)** Elemental energy map. **(c)** Energy filtered STEM (EFSTEM) images for Si, O, Ti, C, and Cu.

a



b

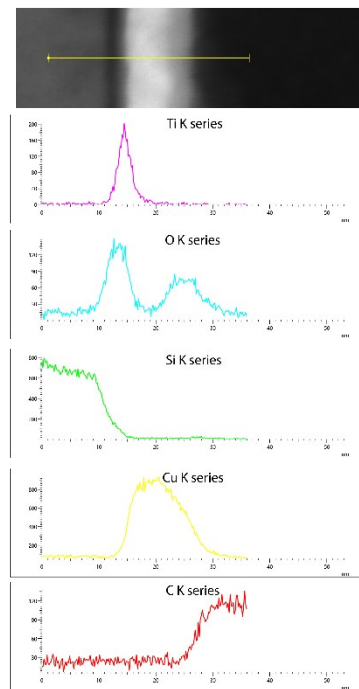


Figure S13. Characterization of MIS sample. (a) Scanning transmission electron microscopy (STEM) image of fresh Cu/TiO₂/p-Si sample with the thicknesses of the various layers. **(b)** STEM energy dispersive x-ray spectroscopy (EDS) for Ti, O, Si, Cu, and C.

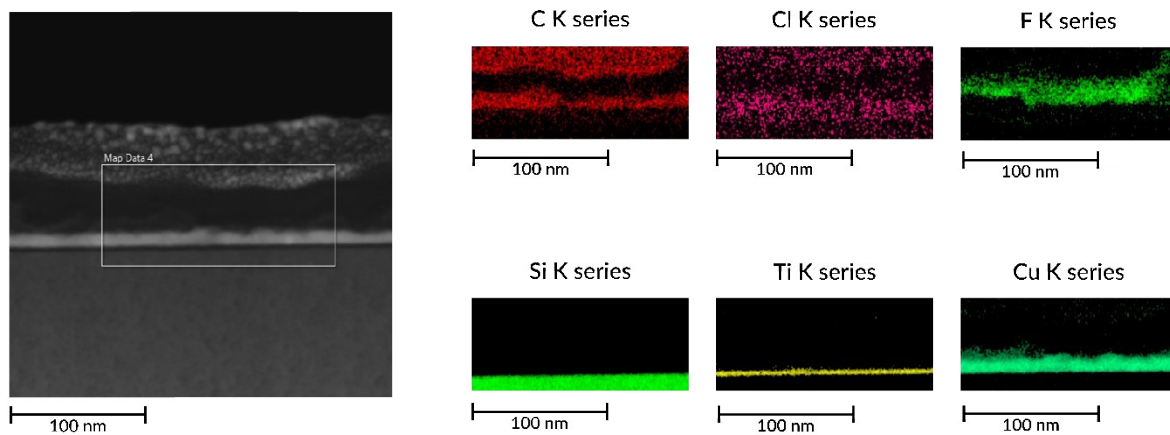


Figure S14. Characterization of Nafion/Sustanion/MIS sample. EDS map of the edge of a Si wafer on to which TiO_2 has been deposited followed by Cu, Sustanion, and Nafion. The TiO_2 layer is identified by the Ti K series data, Sustanion by the Cl K series data, and the Nafion by the F K series data, providing clear evidence for the presence of the Nafion over the Sustanion layer.

Table S1: List of model parameters.

| Reaction | Constant | Units | Ref. |
|-----------------|------------------------|----------------------|------|
| Semiconductor | | | |
| E_g^s | 1.12 | eV | 2 |
| χ_s | 4.05 | eV | 2 |
| ε_s | 11.9 | – | 2 |
| L_s | 300 | μm | |
| m_n^s/m_o | 0.33 | – | 2 |
| m_p^s/m_o | 0.55 | – | 2 |
| μ_n | 1450 | $cm^2 V^{-1} s^{-1}$ | 3 |
| μ_p | 500 | $cm^2 V^{-1} s^{-1}$ | 3 |
| D_n | 4.58×10^{-11} | $mol L^{-1}$ | 3 |
| D_p | 56.281 | s^{-1} | 3 |
| N_a^- | 0.5×10^{19} | cm^{-3} | 4 |
| N_c | 2.8×10^{19} | cm^{-3} | 3 |
| N_v | 10^{19} | cm^{-3} | 3 |
| τ_n | 10 | μs | 3 |
| τ_p | 10 | μs | 3 |
| C_n | 2.8×10^{-31} | $cm^6 s^{-1}$ | 3 |
| C_p | 9.9×10^{-32} | $cm^6 s^{-1}$ | 3 |
| C_{rad} | 1.1×10^{-14} | $cm^3 s^{-1}$ | 3 |
| Interfacial | | | |
| ε_I | 38 | – | 5 |

| | | | |
|-------------|------------|------------|---------|
| m_n^I/m_o | 0.6 | – | 6 |
| m_p^I/m_o | 0.6 | – | assumed |
| ϕ_0 | 0 | eV | assumed |
| ϕ_n^o | 1.2 | eV | 7 |
| ϕ_p^o | 1.18 | eV | 7 |
| ϕ_m | 4.75 | eV | 2 |
| θ_n | 10^{-19} | cm^2 | 8 |
| θ_p | 10^{-19} | cm^2 | 8 |
| ν_{th} | 10^5 | $m s^{-1}$ | 9 |

Although good agreement between theory and experiment exists at low to moderate TiO₂ thicknesses, discrepancy occurs in the absence of a TiO₂ layer (0 nm) and at large TiO₂ thicknesses (≥ 4 nm). With no insulating layer, significant Fermi-level pinning can occur between Cu and Si.² This effect likely leads to the low photovoltages measured experimentally, as seen in Figure 2d in the main text; the current model neglects such Fermi-level pinning because it is not expected to occur once there is an insulating film.^{10–12} At large thicknesses, a high density of trap states, likely from defects in TiO₂, may partially pin the semiconductor Fermi level,² leading to the slightly lower photovoltages measured experimentally than that predicted by theory. We neglect Fermi-level pinning in the model because it is not prevalent near the optimum TiO₂ thickness and is not expected to change the conclusions drawn.^{2,10–12} Other mechanisms, such as Fowler-Nordheim tunneling and Frenkel-Poole emission,² may also become significant at large insulator thicknesses. Alternative transport mechanisms are neglected because they are not expected to occur at the TiO₂ thicknesses relevant to this study; ~ 5 nm is the approximated thickness where contributions of other mechanisms may occur.² We also note that beyond ~ 4 nm of TiO₂ the theoretically predicted photovoltage is independent of TiO₂ thickness because the interfacial trap recombination dominates over tunneling, due to the large tunneling resistance at such large insulator thicknesses; see Figure S5b. Thus, increasing the TiO₂ thickness past ~ 4 nm has negligible impact on the electron concentration and quasi-Fermi level at the semiconductor surface.

We used the measured photocurrent, open circuit photovoltage, and the insulator thickness (presented in Figure 1) with MIS tunnel diode theory equations to approximate the density of interface trap states at the semiconductor-insulator interface (D_{it}).²

$$i = i_{sc} - i_o \left[\exp \left(\frac{qV}{nk_B T} \right) - 1 \right] \quad (\text{S1})$$

$$i_o = k_p \exp \left(-\alpha_p d \sqrt{\phi_p} \right) \exp \left(-\frac{q\phi_b}{k_B T} \right) \quad (\text{S2})$$

All variables are defined in the model description, except for n , which is the ideality factor. D_{it} modifies n and ϕ_b approximately, as given by eqns. S3 and S4:²

$$\phi_b \approx \frac{\varepsilon_i}{\varepsilon_i + q^2 d D_{it}} \phi_b^o + \left(1 - \frac{\varepsilon_i}{\varepsilon_i + q^2 d D_{it}} \right) (E_g - \phi_o) \quad (\text{S3})$$

$$n \approx 1 + \frac{dqD_{it}}{\varepsilon_i} \quad (\text{S4})$$

Combining eq S1–S4 and evaluating them at open-circuit conditions with a root finding algorithm yields the value of D_{it} for a given insulator thickness, photocurrent density, and open circuit photovoltage. The values of all other parameters are defined in Table S1. For a 5 nm TiO₂ thickness, the calculated D_{it} is $4\text{E}13 \text{ eV}^{-1} \text{ cm}^{-2}$ for a photocurrent of 2.0 mA cm^{-2} and a photovoltage of 275 mV. This photocurrent density and photovoltage are approximated from

data presented in Figure 1. This analysis shows that a high density of trap states exists at large TiO₂ thicknesses.¹³ Although this method is approximate, it provides a reasonable estimation of the value of D_{it} .²

An overview of the model is presented here. Readers interested in further details are directed to our previous work.¹⁴ The equations governing steady-state charge carrier transport within the bulk of the semiconductor are given by

$$(\nabla \cdot N_n) = U \quad (\text{S5})$$

$$(\nabla \cdot N_p) = -U \quad (\text{S6})$$

where N_n , N_p , and U are the electron flux, hole flux, and net carrier generation/recombination rate, respectively. The flux of the charge carriers is specified by the drift-diffusion equations

$$N_n = -n\mu_n \nabla V + D_n \nabla n \quad (\text{S7})$$

$$N_p = -p\mu_p \nabla V - D_p \nabla p \quad (\text{S8})$$

where n , p , μ_n , μ_p , D_n , and D_p are the electron concentration, hole concentration, electron mobility, hole mobility, electron diffusivity, and hole diffusivity, respectively. V is the electric potential, which is calculated by Poisson's equation,

$$\nabla \cdot (-\epsilon_r^s \nabla V) = q(p - n + N_d^+ - N_a^-). \quad (\text{S9})$$

where ϵ_r^s , q , N_d^+ , and N_a^- are the relative permittivity of the semiconductor, fundamental charge of an electron, donor doping density, and acceptor doping density. In this study, we consider a p-type semiconductor so the donor doping density is set to zero.

The net rate of charge generation/recombination is a summation of the Shockley-Reed-Hall, Auger, and direct radiative recombination mechanisms subtracted the by the position-dependent generation rate,

$$U = R_{SRH} + R_{Auger} + R_{Rad} - G(x). \quad (\text{S10})$$

The expressions for calculating the various recombination rates are as follows:

$$R_{SRH} = \frac{np - n_i^2}{\tau_p(n + n_i) + \tau_n(p + n_i)}, \quad (\text{S11})$$

$$R_{Auger} = (C_n n - C_p p)(np - n_i^2), \quad (\text{S12})$$

$$R_{Rad} = C_{rad}(np - n_i^2), \quad (\text{S13})$$

where τ_n , τ_p , C_n , C_p , and C_{rad} are the electron lifetime, hole lifetime, electron recombination rate constant, hole recombination rate constant, and carrier recombination rate constant, respectively. Moreover, n_i is the intrinsic carrier concentration,

$$n_i = \sqrt{N_c N_v} \exp\left(-\frac{qE_g^s}{2k_B T}\right). \quad (\text{S14})$$

The carrier generation rate (G) is calculated by integrating over the AM 1.5G solar spectrum (simulated by NREL).

The conduction and valence band energy are determined by

$$E_c = -(\chi_s + V), \quad (\text{S15})$$

$$E_v = -(\chi_s + E_g^s + V). \quad (\text{S16})$$

The quasi-Fermi level levels can be determined through Boltzmann's relation:

$$E_{fn} = E_c + \frac{k_B T}{q} \ln \left(\frac{n}{N_c} \right) \quad (\text{S17})$$

$$E_{fp} = E_v - \frac{k_B T}{q} \ln \left(\frac{p}{N_v} \right), \quad (\text{S18})$$

where k_B , N_c , and N_v are Boltzmann's constant and the effective density of states of electrons and holes, respectively. V_{ph} is defined as the difference in quasi-fermi levels at the semiconductor surface subtracted by the potential drop across the insulator (Δ),

$$V_{ph} = (E_{fn}^{ss} - E_{fp}^{ss}) - |\Delta|. \quad (\text{S19})$$

At the MIS interface, charge carriers must either tunnel into the metal or recombine at interfacial trap sites when at steady state. The tunneling current density is determined through MIS Tunnel Diode Theory initially developed by Card and Rhoderick^{15,16}

$$i_n = -k_n P_{T,n} (n_{ss} - n_{ss}^o) \quad (\text{S20})$$

$$i_p = k_p P_{T,p} (p_{ss} - p_{ss}^o) \quad (\text{S21})$$

$$i_{net} = i_n + i_p \quad (\text{S22})$$

k_n , k_p , $P_{T,n}$, $P_{T,p}$, n^o , and p^o are the electron and hole tunneling rate coefficient, tunneling probability, and equilibrium concentration, respectively. The subscript ss is to denote they are values at the semiconductor surface. Moreover, i_n , i_p , and i_{net} are the electron, hole, and net tunneling current density, respectively. The electron and hole tunneling rate coefficients are calculated as

$$k_n = \frac{4m_n^s \pi q (k_B T)^2}{h^3 N_c}, \quad (\text{S23})$$

$$k_p = \frac{4m_p^s \pi q (k_B T)^2}{h^3 N_v}. \quad (\text{S24})$$

The tunneling probabilities are determined by assuming a rectangular potential tunneling barrier:

$$P_{T,n} = \exp\left(-\alpha_n d \sqrt{\phi_n}\right) \quad (\text{S25})$$

$$P_{T,p} = \exp\left(-\alpha_p d \sqrt{\phi_p}\right) \quad (\text{S26})$$

where α_n , α_p , and d are the electron and hole tunneling coefficients and the insulator thickness, respectively. The tunneling coefficients are calculated by

$$\alpha_n = \frac{4\pi\sqrt{2m_n^I}}{h}, \quad (\text{S27})$$

$$\alpha_p = \frac{4\pi\sqrt{2m_p^I}}{h}, \quad (\text{S28})$$

where m_n^I and m_p^I are the effective electron and hole masses of the insulator. The equilibrium carrier concentrations (n_s^o for electrons and p_s^o for holes) are related to the Schottky barrier as follows.

$$n_s^o = N_c \exp\left(-\frac{q\phi_b}{k_B T}\right) \quad (\text{S29})$$

$$p_s^o = N_v \exp\left(-\frac{q(E_g^s - \phi_b)}{k_B T}\right) \quad (\text{S30})$$

The recombination current density due to interfacial trap sites ($i_{n,R}$ for electrons and $i_{p,R}$ for holes) is approximated by discrete energy levels and are assumed to be of donor type.

$$i_{n,R} = q\theta_n v_{th} N_t \left(n - n f_t - \frac{n_i}{g_D} f_t\right) \quad (\text{S31})$$

$$i_{p,R} = q\theta_p v_{th} N_t (p f_t + g_D (n_i f_t - n_i)) \quad (\text{S32})$$

where θ_n , θ_p , v_{th} , N_t , f_t , and g_D are the average electron and hole capture cross-section, thermal velocity, total number of trap sites, trap site occupation fraction, and the degeneracy factor (assumed to be one), respectively. N_t is calculated by using experimentally measured trap densities (D_{it}),¹⁵ which changes with insulator thickness,

$$N_t = \frac{D_{it}(d)(\psi + V_p - \phi_0)}{f_t}, \quad (\text{S33})$$

where ψ is the band bending potential, V_p is the difference in quasi-fermi level of holes and the valence band energy, and ϕ_0 is the neutral energy level. At steady state, the trap site occupation fraction is determined by enforcing the following constraint.

$$i_{n,R} = i_{p,R} \quad (\text{S34})$$

The potential drop across the insulator (Δ) is calculated in a similar manner as previously reported.¹⁷ The difference we make is in calculating the interfacial capacitance (C), since we take into account the native oxide layer capacitance (C_{ox}).

$$C = \frac{1}{\frac{d}{\varepsilon_I} + \frac{1}{C_{ox}}} \quad (\text{S35})$$

ε_I is the insulator permittivity and C_{ox} is the capacitance of the native oxide, which is a fitted parameter ($1.8 \mu\text{F cm}^{-2}$) in the model because its thickness nor permittivity are well defined. This potential drop reduces the photovoltage driving catalysis and the tunneling and Schottky barrier heights.¹⁸

$$\phi_b = \phi_b^o - \Delta \quad (\text{S36})$$

$$\phi_n = \phi_n^o + \frac{\Delta}{2} \quad (\text{S37})$$

$$\phi_p = \phi_p^o - \frac{\Delta}{2} \quad (\text{S38})$$

where ϕ_b^o , ϕ_n^o , and ϕ_p^o are the idealized barrier heights. The simulation parameters are provided in Table S1.

The governing equations (species material balances, drift-diffusion, and Poisson's equation) were used within the Semiconductor Module and solved with the MUMPS general solver in COMSOL Multiphysics 6.0 with a relative tolerance of 0.0001. The modeling domain was discretized with a nonuniform mesh with refinement near the MIS interface and was comprised of 791 elements. A sensitivity analysis on the mesh size was performed, and the results were found to be independent for meshes greater than the 150 elements.

References

- 1 D. M. King, X. Du, A. S. Cavanagh and A. W. Weimer, *Nanotechnology*, , DOI:10.1088/0957-4484/19/44/445401.
- 2 S. M. Sze and K. K. Ng, *Physics of semiconductor devices*, John Wiley, New York, 3rd edn., 1981.
- 3 COMSOL Multiphysics Software Semiconductor Module.
- 4 J. Quinn, J. Hemmerling and S. Linic, *ACS Energy Lett.*, 2019, **4**, 2632–2638.
- 5 K. Fröhlich, M. Ľapajna, A. Rosová, E. Dobročka, K. Hušeková, J. Aarik and A. Aidla, *Electrochem. Solid-State Lett.*, 2008, **11**, 19–22.
- 6 T. J. Seok, Y. Liu, H. J. Jung, S. Bin Kim, D. H. Kim, S. M. Kim, J. H. Jang, D. Y. Cho, S. W. Lee and T. J. Park, *ACS Nano*, 2018, **12**, 10403–10409.
- 7 M. K. Bera, C. Mahata and C. K. Maiti, *Thin Solid Films*, 2008, **517**, 27–30.
- 8 Ş. Altındal, H. Kanbur, I. Yücedağ and A. Tataroğlu, *Microelectron. Eng.*, 2008, **85**, 1495–1501.
- 9 M. A. Green and J. Shewchun, *Solid State Electron.*, 1974, **17**, 349–365.
- 10 A. Agrawal, N. Shukla, K. Ahmed and S. Datta, *Appl. Phys. Lett.*, 2012, **101**, 042108.
- 11 W. Mönch, *J. Appl. Phys.*, 2012, **111**, 073706.
- 12 D. Connelly, C. Faulkner, P. A. Clifton and D. E. Grupp, *Appl. Phys. Lett.*, 2006, **88**, 3–6.
- 13 A. G. Scheuermann, J. P. Lawrence, A. C. Meng, K. Tang, O. L. Hendricks, C. E. D. Chidsey and P. C. McIntyre, *ACS Appl. Mater. Interfaces*, 2016, **8**, 14596–14603.
- 14 A. J. King, A. Z. Weber and A. T. Bell, *ACS Appl. Mater. Interfaces*, , DOI:10.1021/acsami.2c21114.
- 15 H. C. Card and E. H. Rhoderick, *J. Phys. D. Appl. Phys.*, 1971, **4**, 1589–1601.
- 16 H. C. Card and E. H. Rhoderick, *J. Phys. D. Appl. Phys.*, 1971, **4**, 1602–1611.
- 17 P. Chattopadhyay and A. N. Daw, *Solid State Electron.*, 1986, **29**, 555–560.
- 18 L. C. Olsen, *Solid State Electron.*, 1977, **20**, 741–751.